PROCEEDINGS A

rspa.royalsocietypublishing.org

Research

**Cite this article:** Trinh PH. 2016 A topological study of gravity free-surface waves generated by bluff bodies using the method of steepest descents. *Proc. R. Soc. A* **472**: 20150833. http://dx.doi.org/10.1098/rspa.2015.0833

Received: 8 December 2015
Accepted: 14 June 2016

**Subject Areas:**
fluid mechanics, applied mathematics, integral equations

**Keywords:**
surface gravity waves, wave–structure interactions, wave/free-surface flows, exponential asymptotics, steepest descent, Stokes phenomenon

**Author for correspondence:**
Philippe H. Trinh
e-mail: trinh@maths.ox.ac.uk

Electronic supplementary material is available at http://dx.doi.org/10.1098/rspa.2015.0833 or via http://rspa.royalsocietypublishing.org.

THE ROYAL SOCIETY PUBLISHING

# A topological study of gravity free-surface waves generated by bluff bodies using the method of steepest descents

Philippe H. Trinh

Oxford Centre for Industrial and Applied Mathematics, Mathematical Institute, University of Oxford, Oxford OX2 6GG, UK

PHT, 0000-0003-3227-1844

The standard analytical approach for studying steady gravity free-surface waves generated by a moving body often relies upon a linearization of the physical geometry, where the body is considered asymptotically small in one or several of its dimensions. In this paper, a methodology that avoids any such geometrical simplification is presented for the case of steady-state flows at low speeds. The approach is made possible through a reduction of the water-wave equations to a complex-valued integral equation that can be studied using the method of steepest descents. The main result is a theory that establishes a correspondence between different bluff-bodied free-surface flow configurations, with the topology of the Riemann surface formed by the steepest descent paths. Then, when a geometrical feature of the body is modified, a corresponding change to the Riemann surface is observed, and the resultant effects to the water waves can be derived. This visual procedure is demonstrated for the case of two-dimensional free-surface flow past a surface-piercing ship and over an angled step in a channel.

## 1. Introduction

Let us consider the problem of determining the steady surface gravity waves generated by a body moving in a two-dimensional potential fluid. At the free surface, $y = \eta(x)$, Bernoulli's equation requires that

$$\tfrac{1}{2}q^2 + g\eta = \text{const.}, \tag{1.1}$$

where $q$ is the fluid speed and $g$ is the gravitational parameter. The nonlinearity of (1.1) forms the primary

difficulty of analysis; in order to make any sort of progress, the equation must usually be linearized. As explained by Tuck [1], this linearization will typically involve making one of two possible assumptions.

In the first, the relevant flow quantities are expressed as a series expansion in powers of a geometric parameter such as

$$\delta = \frac{\text{body size}}{\text{depth of submergence}}. \tag{1.2}$$

For instance, one might assume that at leading order, the object is asymptotically thin or streamlined in one or several of its dimensions, or that the body is submerged at great depth compared with its dimensions. Then, in the $\delta \to 0$ limit, the solution is linearized about uniform flow.

However, approximation schemes that are dependent on taking an asymptotic limit of some geometric parameter can be difficult to justify formally, because the boundary conditions are typically imposed at approximate locations rather than at exact locations. For example, flow past a circular cylinder can be approximated by flow past a dipole, but a finite-order approximation (in powers of the cylinder radius) can never yield a closed streamline around the body (see e.g. fig. 1 of [1]). Similar examples occur in a variety of geometrically perturbed problems (see e.g. the discussion on p. 542 of Wexler *et al*. [2]). Even beyond the inability to satisfy the exact body conditions, another limitation of such approximations is that little can be said about the flow around geometrically nonlinear or bluff bodies; this is a crucial limitation for our purposes.

The second linearization of (1.1) is more suitable for developing a theory of waves created by thick or bluff bodies. In this approach, the relevant small parameter is typically related to the Froude number, $Fr$, and introduced in this work as

$$\epsilon = Fr^2 = \frac{\text{inertial}}{\text{gravitational forces}}. \tag{1.3}$$

There has been much recent interest in studying how high-Froude effects modify the standard Kelvin ship-wave pattern [3,4]. However, while the $\epsilon \to \infty$ limit forms an interesting regime in its own right, the hull geometry plays a less vital role in the analysis at leading order (cf. [5]). We shall instead concentrate on the problem as $\epsilon \to 0$, where the body is assumed to move at low speeds, and the free surface is entirely flat at leading order. The great advantage of this approach is that there is no geometrical restriction placed on the body; thus, the associated boundary conditions are satisfied exactly to all orders. The challenge, however, is that the limit $\epsilon \to 0$ is singular, and the free-surface waves are exponentially small, with amplitudes that scale as $\mathrm{e}^{-\text{const.}/\epsilon}$. Thus, they are said to be beyond-all orders of any regular expansion in powers of $\epsilon$. The inability to detect the surface waves using standardized methods is known as Ogilvie's low-Froude paradox [6,7].

In the 50 years following Ogilvie's work, the low-Froude paradox was eventually resolved through the combined efforts of many researchers, and a review of the historical progression can be found in [7,8]. Chapman & Vanden-Broeck [9] were the first, to the best of our knowledge, to derive the correct leading-order wave solution of the low-Froude problem, and their approach uses exponential asymptotic techniques of matched asymptotics and Stokes line smoothing [10,11].

For the particular case of gravity-driven flow, there is a fortuitous simplification of the water-wave equations that allows the $\epsilon \to 0$ limit to be studied under a more geometrical framework. The derivation of this framework is the topic of a companion paper [8]. There it is shown that, by extending earlier ideas by Tulin [12] and Tuck [13], solutions can be expressed in the form of a (nearly explicit) integral. Although the study of this integral is not straightforward, additional simplifications can be made so as to produce an asymptotic approximation of the surface waves via the method of steepest descents. Although integral approximation techniques in exponential asymptotics are well known [14–17], the approach in reference [8] had not yet been done for the study of low-Froude free-surface flows.

While the companion work [8] explains how the approximation procedure is performed for general wave-body configurations, in this work, we study the intricacies of the method when

applied to particular concrete flow geometries. In particular, we shall demonstrate how the framework can be applied for the particular cases of flow past an angled step in a channel and flow past a surface-piercing obstruction. The main result is a procedure that allows us to directly relate the geometry of the physical flow to certain Riemann surfaces connected to the analysis. We first provide a brief review of the main results of the companion paper [8].

## 2. The reduced water-wave equations

As a preliminary example, consider potential steady free-surface flow past the stern of a surface-piercing ship, modelled as a two-dimensional semi-infinite body (figure 1). The physical coordinates are denoted by $z = x + \mathrm{i}y$, and the complex potential is written as $w = \phi + \mathrm{i}\psi$, for velocity potential, $\phi$, and streamfunction, $\psi$. Our task is to solve for the speed, $q(\phi, \psi)$, and streamline angle, $\theta(\phi, \psi)$, on the free surface, where $\phi > 0$ and $\psi = 0$. The governing water-wave equations are reviewed in appendix A, and are given in non-dimensional form by

$$\epsilon q^2 \frac{\mathrm{d}q}{\mathrm{d}\phi} + \sin\theta = 0 \quad \text{and} \quad \log q = \frac{1}{\pi}\int_{-\infty}^{0} \frac{\theta(\varphi)}{\varphi - \phi}\mathrm{d}\varphi + \mathscr{H}\theta(\phi) \quad \text{on } \psi = 0, \tag{2.1}$$

where we have introduced the Hilbert transform operator for the principal-value integral

$$\mathscr{H}\theta(\phi) = \mathscr{H}[\theta] = \frac{1}{\pi}\int_{0}^{\infty} \frac{\theta(\varphi)}{\varphi - \phi}\mathrm{d}\varphi. \tag{2.2}$$

The first equation in (2.1) is the differentiated form of Bernoulli's equation with $\epsilon = Fr^2 = U^2/(gL)$ being the square of the Froude number for upstream speed $U$, gravity $g$, and geometrical length scale $L$. The second is a boundary-integral equation, written so as to split the integral on the solid body ($\phi < 0$), where $\theta$ is assumed to be known, with the Hilbert transform over the free surface ($\phi > 0$), where $\theta$ is unknown. For the surface-piercing configuration, we also specify that the free surface attaches to the body at a stagnation point, $q(0) = 0$.

For the semi-infinite ship with the single stern-face of angle $\pi\sigma$ in figure 1, the problem is non-dimensionalized, so that the corner lies at $\phi = -1$. The body is then specified as

$$\theta_{\text{ship}} = \begin{cases} 0 & \text{for } \phi \in (-\infty, -1), \\ \pi\sigma & \text{for } \phi \in (-1, 0). \end{cases} \tag{2.3}$$

The above body shape is then used in (2.1), and the two equations can be numerically solved using the finite-difference schemes discussed in [18,19]. A typical numerical solution for the case of a rectangular stern, $\sigma = 1/2$, is shown in figure 1*a* at $\epsilon = 1$, where we have plotted the physical free surface height, $y(x)$, obtained by integrating the relation $\mathrm{d}w/\mathrm{d}z = q\,\mathrm{e}^{-\mathrm{i}\theta}$. The speed, $q$, on the free surface is shown in figure 1*b*.

Although the two-dimensional semi-infinite geometry of (2.3) may seem rather idealized, it presents a canonical model of wave–structure interaction with a variety of numerical and analytical challenges. These two-dimensional stern hull shapes have been considered in, for example, the works of [18,20], but similar considerations can be extended to ships with multiple corners [21], or ships with smooth or bulbous profiles [22].

The global nature of the Hilbert transform presents a major difficulty in solving (2.1). Earlier, Tuck [13] had proposed the idea that toy models of certain wave–structure problems could be derived by ignoring or replacing the Hilbert transform, and changing (2.1) to an initial-value differential equation. In the companion paper [8], such a reduction was shown to be formally possible in the limit $\epsilon \to 0$. The argument is as follows.

Let us expand the solution of (2.1) as a truncated regular series expansion and an error term

$$q = \sum_{n=0}^{N-1} \epsilon^n q_n + \bar{q} \quad \text{and} \quad \theta = \sum_{n=0}^{N-1} \epsilon^n \theta_n + \bar{\theta}. \tag{2.4}$$

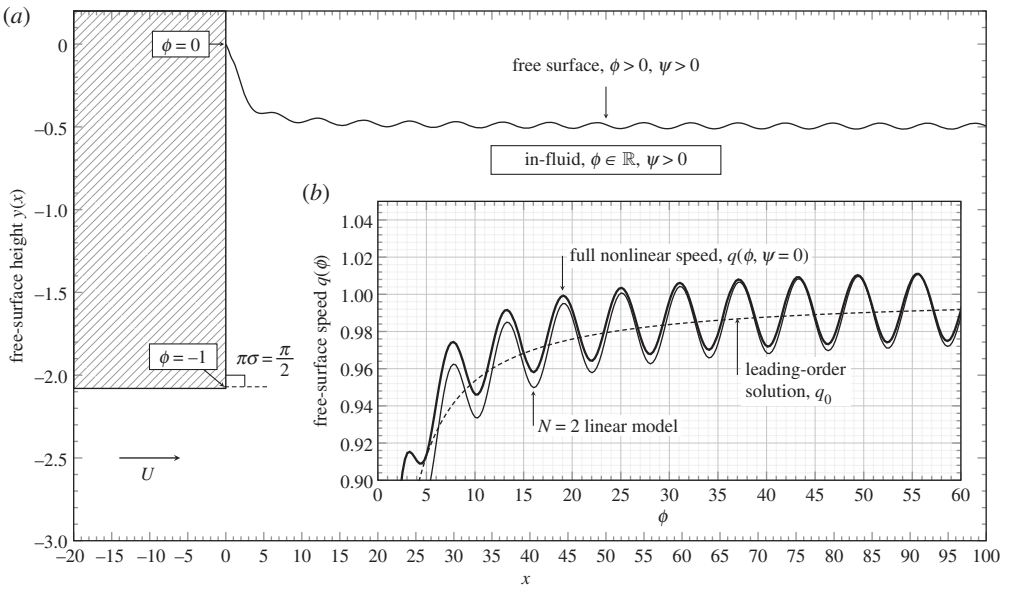


**Figure 1.** Flow past the stern of the rectangular ship (2.3) with $\sigma = 1/2$. The surface profile, $y(x)$, in (*a*) corresponds to a solution of the full nonlinear equations (2.1) at $\epsilon = 1.0$ using the numerical scheme of Trinh *et al*. [18]. The profiles in (*b*) correspond to the surface speed, $q$, as a function of the potential, $\phi$. In this inset, the full solution (shown thick) is compared with the leading-order approximation, $q_0$, in (2.5) (shown dashed), and a solution of the linear model spanning (A 6) and (A 7) (shown thin).

It follows from setting $\epsilon = 0$ in (2.1) that at leading order, $\theta_0 = 0$, and the free-surface is entirely flat. Effectively, the surface has been replaced by a rigid plane, and the solution is known as the double-body flow. In this case, the leading-order speed is given by

$$q_0 = \left(\frac{\phi}{\phi + 1}\right)^{\sigma}. \tag{2.5}$$

As seen in figure 1*b*, the leading-order solution fails to capture the wave phenomena. In fact, the situation is much worse, and it can be argued through the study of higher-order terms in (2.4), that none of the terms, $q_n$ and $\theta_n$, will contain an oscillatory component at any order.

Let us take $q$ and $\theta$, defined on the free surface, $\phi > 0$, and analytically continue the solutions to complex values of $\phi$. Relabelling $\phi \mapsto w \in \mathbb{C}$, the system (2.1) can be reduced to the following complex-valued differential equation

$$\epsilon \frac{\mathrm{d}\bar{q}}{\mathrm{d}w} + \left[\frac{\mathrm{d}\chi}{\mathrm{d}w} + \epsilon \frac{\mathrm{d}P_1}{\mathrm{d}w}\right]\bar{q} \sim R(w; \hat{\mathscr{H}}[\bar{\theta}]), \quad \text{where } \hat{\mathscr{H}}\bar{\theta}(w) = \hat{\mathscr{H}}[\bar{\theta}] = \int_0^{\infty} \frac{\bar{\theta}(\varphi)}{\varphi - w}\mathrm{d}\varphi. \tag{2.6}$$

The derivation of equation (2.6) is reviewed in appendix A.

In (2.6), we have assumed that $w$ lies in the upper half-plane (an analogous derivation can be done for the lower half-plane). We have also introduced $\hat{\mathscr{H}}$ for the complexified Hilbert transform, which is non-singular for $w$ off the real axis. The two functions, $\chi$ and $P_1$, (2.6) are known, typically in closed form, whereas $R$ may be approximated; these quantities will be specified in §3 and in appendix A. Integrating the equation, and taking the limit whereby we return to the physical free surface, $w \to \phi > 0$, we obtain the result of

$$\bar{q}(\phi) \sim \left[\frac{\mathrm{e}^{-P_1(\phi)}}{\epsilon}\right]\left[\int_{\phi_{\mathrm{start}}}^{\phi} R(\varphi; \hat{\mathscr{H}}[\bar{\theta}])\mathrm{e}^{P_1(\varphi)}\,\mathrm{e}^{\chi(\varphi)/\epsilon}\mathrm{d}\varphi\right]\mathrm{e}^{-\chi(\phi)/\epsilon}. \tag{2.7}$$

In the example of flow past a surface-piercing ship, we take $\phi_{\mathrm{start}} \to 0$ in order to account for condition of a stagnation point, $\bar{q}(0) = 0$, at the edge of the hull.

In the limit $\epsilon \to 0$, the initial contour of $\varphi \in [\phi_{\text{start}}, \phi]$ in (2.7) can be deformed along paths of steepest descent. Once done, an asymptotic expansion of the integral is derived by consideration of dominant contributions from the endpoints, as well as any relevant saddle or critical points of the integrand. In reference [8], it is shown that the endpoint contributions lead to a re-expansion of higher-order algebraic terms from (2.4), whereas the exponentially small water waves are caused by contributions away from the positive real axis. Therefore, $\hat{\mathscr{H}}[\bar{\theta}]$, which only depends on the free surface values of $\bar{\theta}$, can be ignored at leading order. This subtle reduction process explains why certain reduced wave models may remove or substitute alternatives for the Hilbert transform.

Let $q_{\text{exp}}$ be the exponentially small waves that arise from the integral (2.7) according to the above process. The free surface will then be approximated by

$$q \sim [q_0 + \epsilon q_1 + \mathcal{O}(\epsilon^2)] + 2\text{Re}(q_{\text{exp}}), \tag{2.8}$$

which includes both the wave-free flow (the square-bracketed terms) and the surface waves. We are required to add both $q_{\text{exp}}$ from (2.7) and also its complex conjugate, owing to an analogous argument for the analytic continuation of (2.6) into the lower half-plane, and subsequent application of the Schwartz reflection principle. Combining these two contributions then leads to $2\text{Re}(q_{\text{exp}})$.

We now provide a numerical example. Suppose we return to the differential equation (2.6) and, having been sufficiently convinced by the above arguments, we ignore the $\hat{\mathscr{H}}[\bar{\theta}]$ contributions to $R$. Using the initial condition $\bar{q}(0) = 0$, the values (A 6*b*) and (A 6*c*) for $\chi$ and $P_1$, and the approximation (A 7) for $R$, the differential equation is solved as an initial-value problem. The result, (2.8), is shown in figure 1*b*. The agreement with the full nonlinear solution is superb even at the moderate value of $\epsilon = 1$. At this value of $\epsilon$, the approximate wave amplitude in figure 1*b* is $1.6 \times 10^{-2}$ for the full model, and $1.9 \times 10^{-2}$ for the linear model, and thus, a relative error of $\approx 18\%$. If $\epsilon$ is decreased to 0.5, the relative error decreases to $\approx 3.6\%$. In reference [8], a careful check of numerical versus asymptotic results verifies these claims properly.

In reference [8], the asymptotic approximation of the integral (2.7) is made based on the general assumption that the initial contour of integration can be deformed for any given body geometry, and that such a deformation generically includes the key critical points generating the water waves. In actuality, the topology of the steepest descent paths may be rather complicated. For example, different body geometries may yield different contributing singularities, or modifications of the geometry may require routing the descent trajectories onto further Riemann sheets. The purpose of this work is to explore these issues, and to provide a more detailed study of the correspondence between a given physical hydrodynamical flow and the topology of the associated steepest descent paths.

## 3. Computation of the Riemann surfaces

We now explain how the Riemann surfaces connected to the steepest descent paths are computed. Integral (2.7) is first re-written as

$$I(\phi) = \int_{\phi_{\text{start}}}^{\phi} f(\varphi) \mathrm{e}^{\chi(\varphi)/\epsilon} \mathrm{d}\varphi, \quad \text{where } f(\varphi) = R(\varphi; \hat{\mathscr{H}}[\bar{\theta}]) \mathrm{e}^{P_1(\varphi)}. \tag{3.1}$$

The exponential argument, $\chi$, is given by (A 6*b*) and repeated here as

$$\chi(w) = \int_{w_0}^{w} \frac{\mathrm{ij}}{q_0^3(\varphi)} \mathrm{d}\varphi. \tag{3.2}$$

In the definition of $\chi$, we have introduced the sign constant, j. The constant takes the value $\mathrm{j} = 1$ for surface-piercing flows and $\mathrm{j} = -1$ for channel flows. As explained in (A 4), this distinction is necessary owing to the difference in surface flow direction relative to the solid body. The function $q_0$ in (3.2) is the double-body solution discussed in §2, and encodes the information of the geometry. Any choice for the initial point of integration, $w_0$, is valid so long as the integral is

defined, and different choices are compensated by the numerical pre-factors associated with $f(\varphi)$. We will discuss specifics of the $\chi$ function later.

Returning to (3.1), the contour is initially along the real axis, $\varphi \in [\phi_{\text{start}}, \phi]$, but once it is deformed along the paths of steepest descent, this would yield the general decomposition of

$$I(\phi) \sim I_{\text{endpt}}(\phi) + I_{\text{exp}}. \tag{3.3}$$

Thus, the integral is approximated by the two endpoint contributions, $I_{\text{endpt}}$, from $\varphi = \{\phi_{\text{start}}, \phi\}$, and further contributions, $I_{\text{exp}}$, from critical points (saddle points, poles or branch points), presumed to correspond to the surface waves. Paths of steepest descent lie along level sets of $\text{Im}(\chi)$. Thus, the criteria for determining whether $w$ lies on the steepest descent path from $w_0$ are

$$\text{Im}[\chi(w)] = \text{Im}[\chi(w_0)] \quad \text{and} \quad \text{Re}[\chi(w)] \leq \text{Re}[\chi(w_0)]. \tag{3.4}$$

The first condition ensures that $w$ is on a path of steepest descent or ascent; the second ensures that it is, in fact, on a path of steepest descent.

In practice, however, calculating $\chi(w)$ for different values of $w$ is not necessarily straightforward, as depending on the body function, $q_0$, $\chi$ may possess a complicated branch structure. A similar issue was encountered in the development of asymptotic solutions to the problem of thin-film rupture [23]. In order to explain the terminology for the branch structure, let us return to the example ship flow of §2. Substituting $q_0$ from (2.5) into (3.2), and choosing the initial point of integration, $w_0 = -1$, to correspond to the corner of the ship, we have

$$\chi(w) = \chi_{(k_1,k_2)} = \text{i} \int_{-1}^{w} \left( \frac{\varphi + 1}{\varphi} \right)^{3\sigma} \text{d}\varphi. \tag{3.5}$$

To define a single-valued function for the above integral, we must specify the branches and branch cuts associated with the two critical points at $\varphi = W_i \in \{-1, 0\}$. Depending on the choice of integration contour in (3.1), the contour may cross a branch cut where the single-valued specification of $\chi$ in (3.2) encounters a discontinuity. For our purposes, we wish to continue the trajectory of the specified steepest descent paths of (3.1) beyond such discontinuities. In other words, when a branch cut is traversed, we will move onto the adjacent Riemann sheet, and take the values of $\chi$ from the next branch. Together, the collection of Riemann sheets forms the Riemann surface for $\chi$.

Continuing with our ship example in (3.5), let us choose the branch cuts so that each lies along a ray of constant angle from the respective branch point, $w = W_i$. Let $k_i \in \mathbb{Z}$ be the winding number around the point $W_i$—that is, $k_i$ marks the number of rotations associated with a given analytic continuation around $W_i$, with positive and negative integers for anticlockwise and clockwise rotations, respectively. Each distinct branch of $\chi$ is then associated with the pair $(k_1, k_2)$ indicating the number of revolutions required in order to reach the current branch from the principal branch. For example, consider the surface-piercing ship with branch points at $W_1 = -1$ (the corner) and $W_2 = 0$ (the stagnation point). Three illustrative branches are labelled as

$$\chi_{(0,0)}, \quad \chi_{(0,1)} \quad \text{and} \quad \chi_{(0,1)\to(1,1)}. \tag{3.6}$$

The first, $\chi_{(0,0)}$, is the principal branch obtained by integrating (3.5) from $\varphi = -1$ to $\varphi = w$ without crossing a branch cut. The second, $\chi_{(0,1)}$, is found by integrating from $\varphi = -1$, then circling the stagnation point, $W_2$, in the positive sense, and arriving at $\varphi = w$. The third, $\chi_{(0,1)\to(1,1)}$, begins from the $\chi_{(0,1)}$ branch, and then performs an additional rotation about the corner, $W_1$. When it may be ambiguous, we use the arrow notation to clarify the order in which branch cuts are crossed.

A three-dimensional cross section of the Riemann surface can be visualized by plotting $(\text{Re}\, w, \text{Im}\, w, \text{Re}\, \chi)$, using the values of $\chi_{(0,0)}$ and its adjacent sheets. In general, these surfaces will self-intersect within the graphical representation, but they are otherwise free of discontinuities. For similar visualizations of Riemann surfaces connected to problems in fluid mechanics, see the work by Crew & Trinh [24] where the Riemann surfaces associated with travelling waves of permanent form (Stokes waves) are explained.

The Riemann surfaces that appear in this paper are graphed from numerical integration of $\chi$ in (3.2) using the trapezoid rule. In such computations, we have carefully defined the locations of the branch cuts, and implemented a numerical scheme that allows the integration path to switch smoothly between the individual branch sheets. The coordinate data for the Riemann surfaces in this paper can be found within the electronic supplementary material.

## 4. The paths of steepest descent

We are now ready to study the steepest descent paths associated with the integral (3.2). We have chosen to focus on flow past three representative geometries: a ship's stern modelled as a semi-infinite rectangular body in infinite depth in §4a, a rectangular step in a channel in §4b and an angled step in a channel in §4c. The methods we present can be extended to cover many other classes of moving bodies, notably those for which a boundary-integral formulation exists [19].

### (a) The rectangular ship in infinite depth

Let us return to the case of flow past the semi-infinite rectangular stern first introduced in §2. The geometry is specified by $\theta_{\text{ship}}$ in (2.3) with $\sigma = 1/2$, and the leading-order speed is given by (2.5). Our task is to approximate the integral (3.1), which involves the function $\chi$ in (3.5). The critical points in the $w$ or $\varphi$-plane include the corner $w = -1$ and the stagnation point $w = 0$, and the branch cuts from both are taken along the positive real axis.

In the integral (3.1), we would like to take the initial point of integration to be the stagnation point, $\phi_{\text{start}} = 0$, so as to use of the boundary condition $\bar{q}(0) = 0$. However, because the origin is a degenerate point, it is easier to first consider the descents paths for the integral

$$I(\phi) = \int_{\text{A}}^{\phi} f(\varphi) \mathrm{e}^{\chi(\varphi)/\epsilon} \mathrm{d}\varphi, \tag{4.1}$$

where $\varphi = \text{A}$ is a small and positive number. In all the geometries considered in this work, it can be verified that $f(\varphi)$ contains only algebraic dependence on $\epsilon$, and thus the steepest descent contours will only depend on $\chi$. Below, we use $w$ interchangeably with $\varphi$ (the dummy variable).

Using the methodology outlined in §3, we generate the Riemann surface associated with $\chi$, and the result is shown in figure 2. The visualized surface is composed of the three listed branches in (3.6). In the rectangular ship geometry, the adjacent Riemann sheets arising owing to rotations about the corner point are untouched by the relevant steepest descent paths. This will not always be the case for all geometries; in both the examples of a rectangular and angled step in §4b,c, the steepest descent contours will, indeed, traverse onto adjacent Riemann sheets.

We continue to examine figure 2, but now turn our attention to the planar projection, shown in grey, where several constant phase curves, $\text{Im}(\chi) = \text{const.}$, are projected down from the Riemann surface. The dashed lines are constant phase lines emerging from the corner point, $w = -1$, with one set of lines, on the right, forming a homoclinic, and the other, on the left, forming an open triangular region. Setting $w + 1 \sim r\mathrm{e}^{\mathrm{i}\vartheta}$ and $\text{Im}\,\chi = 0$ in (3.5), we find that the homoclinic is formed by the two local angles, $\vartheta = \pm 2\pi/5$, whereas the left triangular region is formed by the two local angles, $\vartheta = \pm 4\pi/5$.

Along the dashed curve emerging at a local angle of $\vartheta = 2\pi/5$, we have $\text{Re}\,\chi \geq 0$, which indicates that the trajectory along this curve lies uphill of the point $w = -1$ (note that $\chi$ in (3.5) was defined, so that $\chi = 0$ at the corner). In figure 2, two steepest descent trajectories are shown with thick solid lines. For the trajectory that begins in the interior of the homoclinic, the descent path forms an arc that tends towards $w = 0$ in a direction tangential to the negative real axis. For the trajectory that begins exterior of the homoclinic and to the right of the plane, the path moves to $|w| \to \infty$ along the dashed curves, marking the triangular region. The dashed curves, called the *Stokes lines*, mark the critical curves across which the steepest descent paths change in dramatic fashion; they are of key importance in what follows.

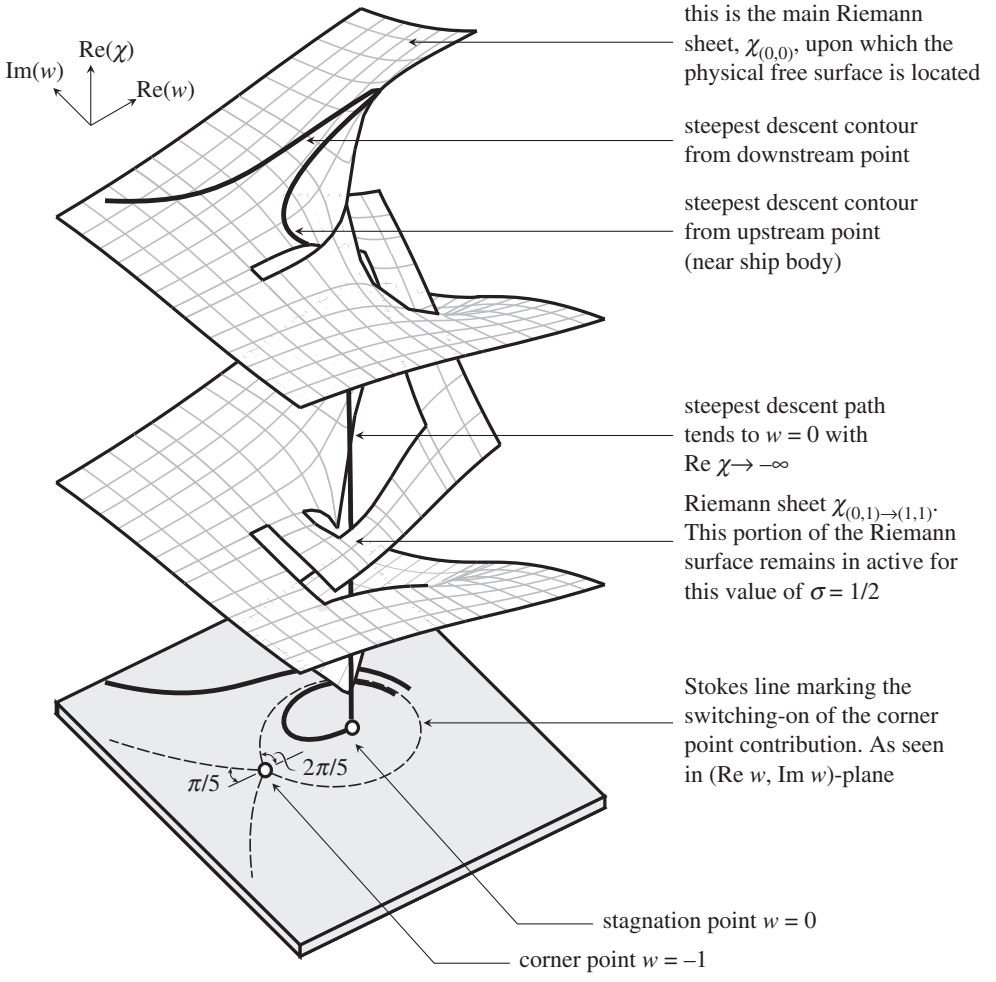


**Figure 2.** Riemann surface of $\chi$ for the rectangular ship geometry with $\sigma = 1/2$ as shown in the (Re $w$, Im $w$, Re $\chi$)-plane. The two critical points are $w = W_i = \{-1, 0\}$. The Riemann sheets are labelled $\chi_{(k_1,k_2)}$ for the respective winding numbers, $k_j$. The two thick contours correspond to steepest descent trajectories for an upstream point (near $w = 0$) and a downstream point, both on the free surface. The bottom plane shows the projection of curves onto the (Re $w$, Im $w$)-plane, with dashed lines indicating the contour Im $\chi = 0$ from the corner point. The surface is generated from numerical integration of (3.5). Data and further visualizations of the surface are found in the electronic supplementary material.

## (i) Only endpoint contributions

Consider the integral (4.1) with initial and final points, $\varphi = \mathrm{A}$ and B, both chosen to lie sufficiently close to the stagnation point of the ship, and hence within the dashed homoclinic of figure 2.

The steepest descent process is sketched in figure 3*a*. We see that the contour from $\varphi = \mathrm{A}$ is deformed in an anticlockwise manner and tends to $\varphi = 0$, where Re $\chi \to -\infty$. Within this valley, the contour then unwinds clockwise, with $\chi$ increasing until arriving at $\varphi = \mathrm{B}$. Thus, when the integral, $I(\phi)$, is evaluated at $\phi = \mathrm{B} < \mathrm{B}^*$, where $\mathrm{B}^*$ marks the intersection of the dashed line with the positive real axis, the result of this process yields two dominant endpoint contributions, written loosely as

$$I(\phi) \sim I_{\mathrm{endpt}}, \tag{4.2}$$

the terms of which can be derived by integrating (4.1) by parts. As shown in [8], this process yields the higher-order algebraic corrections in (2.4).

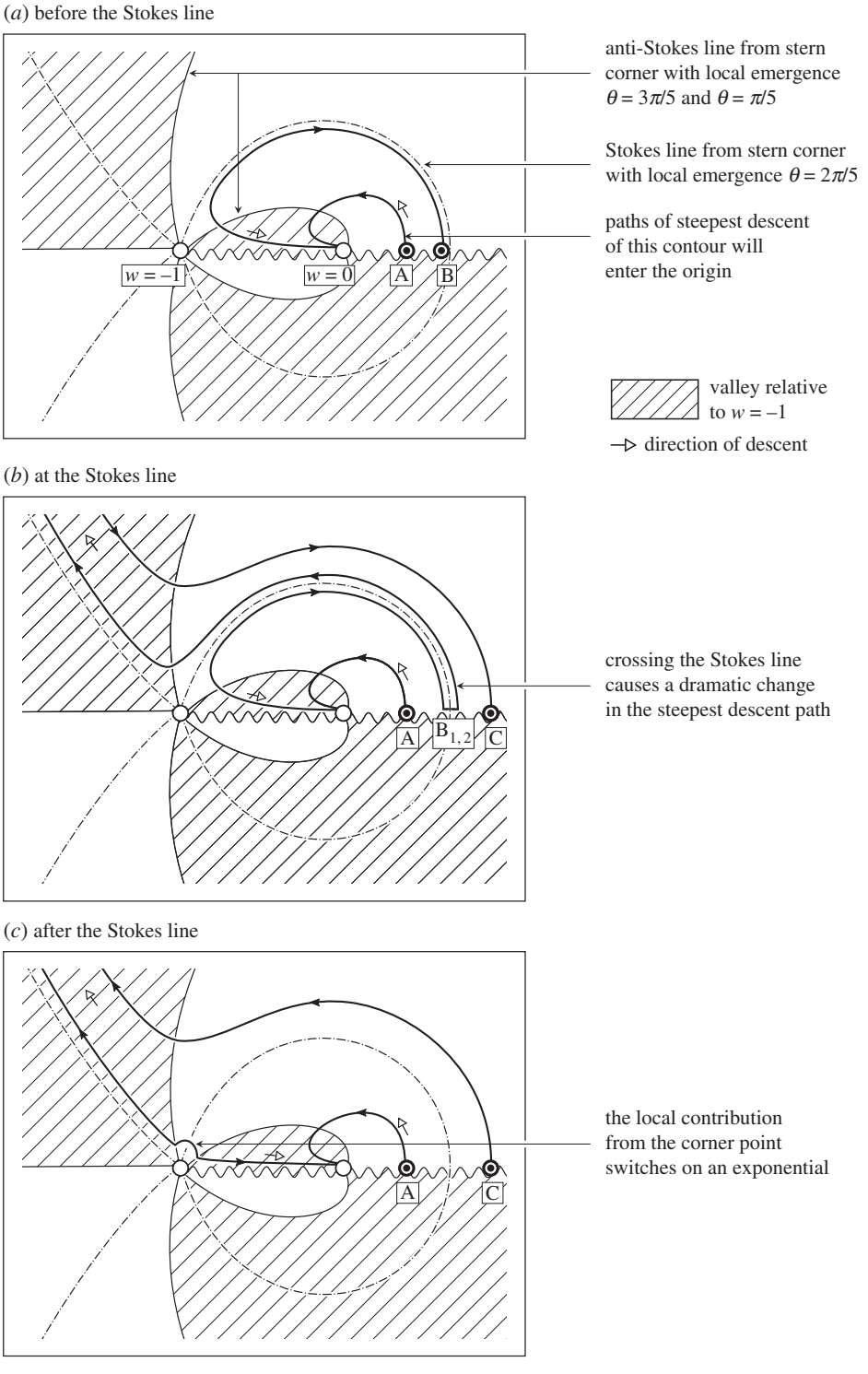


**Figure 3.** Illustration of the steepest descents deformation process for the integral (4.1), as drawn in the (Re $w$, Im $w$)-plane (for dummy integration variable $\varphi$). The endpoints of the contour are marked as a dark circle, and run from A to B in (*a*) or A to C in (*b*, *c*). Branch cuts are shown as a wavy line. The open circles indicate the two critical points $w = W_i = \{-1, 0\}$. Black arrows along the thick lines indicate the integration direction, whereas white arrows indicate the local direction of descent.

Now that we have understood the approximation process, we may freely take $A \to 0$, that is, take the initial point of integration in (4.1) to the stagnation point. Then, the proper steepest descent deformation for the contour $\varphi \in [0, B]$ involves only the single contour in the upper half-plane connected to B.

*For points sufficiently close to the body of the ship, we conclude that there are no free-surface waves in the limit $\epsilon \to 0$ (to this order of exponential accuracy).*

### (ii) Crossing the Stokes line

The dashed curve in figure 3*a* is known as the *Stokes line*, and it marks the critical curve across which the analytic continuation of the integral, $I(\phi)$, switches-on a subdominant contribution. The intersection of the Stokes line with the original contour along $\varphi \in [A, \phi]$, is the location across which the deformation process makes a dramatic topological change, and this occurrence is known as the *Stokes phenomenon* [25]. Consider the method of steepest descents applied to an initial contour in (4.1) beginning at $\varphi = A$ and ending at $\varphi = \phi = C$. The point C is chosen to be sufficiently far downstream so as to pass the Stokes line; hence, it lies outside of the homoclinic region. This is sketched in figure 3*b*. Conceptually, it is easier to split the integration range, so that

$$I(C) = \left( \int_A^{B_1} + \int_{B_2}^{C} \right) f(\varphi)\, e^{\chi(\varphi)/\epsilon} d\varphi, \tag{4.3}$$

where $B_1$ and $B_2$ are the limiting points just on the interior and exterior of the homoclinic orbit.

The deformed contour is sketched in the figure. The steepest descent contours from $\varphi = A$ and $B_1$ are the same as before, with both curves unravelling within the dashed homoclinic and then connected by the valley at $\varphi = 0$, where $\chi \to -\infty$. However, for the second integral in (4.3), the contours from $\varphi = B_2$ and C tend to the valley in the upper left, as $|\varphi| \to \infty$. Because the two integrals that run alongside the top of the homoclinic orbit will sum to zero, this leaves the final deformed contour in figure 3*c*. Thus, in addition to the endpoint contributions (4.2), we have

$$I(\phi) \sim I_{\text{endpt}} + I_{\text{exp}} = I_{\text{endpt}} + \oint\!\!\!\!\!\!\circlearrowleft_{\varphi=-1} f(\varphi) e^{\chi(\varphi)/\epsilon} d\varphi. \tag{4.4}$$

The evaluation of the $\oint\!\!\!\!\!\!\circlearrowleft$ integral along the steepest descent path depends only on the local properties of the integrand near $\varphi = -1$. This is why we may think of the surface waves as being generated by the ship's corner. The analytical form of (4.4) is given in [8].

*For points sufficiently far downstream from the body, we conclude that the free-surface waves arise from switching-on the saddle–point contribution owing to the corner of the ship (the Stokes phenomenon).*

## (b) The rectangular step in a channel

Consider now the case of channel flow past a step of angle $\pi\sigma > 0$, as illustrated in figure 4*a*. The problem is non-dimensionalized, so that in the complex potential plane, $w = \phi + i\psi$, the free surface is along $\psi = 0$, the channel bottom is along $\psi = -\pi$ and $-\infty < \phi < \infty$. In order to develop the analogous formulae to (2.1), we map the $w$-plane to the upper half $\zeta$-plane using

$$\zeta = \xi + i\eta = e^{-w}. \tag{4.5}$$

This is shown in figure 4*b*. Within the $\zeta$-plane, the solid boundary lies along $\xi \le 0$, the free surface along $\xi \ge 0$, and downstream infinity corresponds to $\zeta \to 0$. Bernoulli's equation and the boundary-integral equation are given in (A 2) with $j = -1$. Further details of this set-up are given in appendix A.

Having non-dimensionalized with the channel height, we have the freedom to specify the locations of the stagnation point, $\zeta = -b$, and corner, $\zeta = -a$, with $0 < a < b$. The body geometry

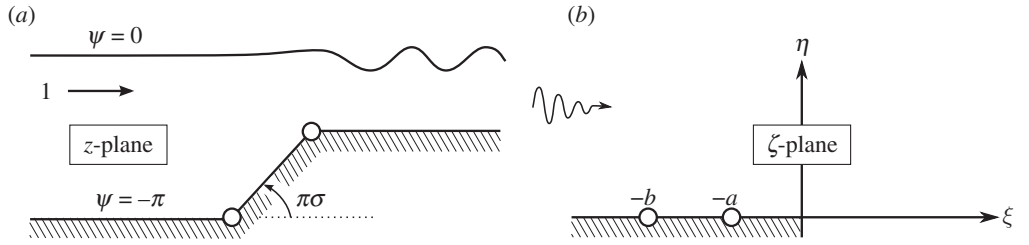


**Figure 4.** Physical $z$-plane ($a$) and upper-half $\zeta$-plane ($b$) for the non-dimensional flow over a step of angle $\pi\sigma$. The flow is contained within a strap in the complex potential $w$-plane. The map from the $w$-plane to the upper-half $\zeta$-plane is given by $\zeta = \mathrm{e}^{-w}$. The points $\zeta = -b$ and $-a$ correspond to the stagnation point and corner, respectively.

is then described by the respective angle and speed,

$$\theta_{\text{step}} = \begin{cases} 0 & \xi \in (-\infty, -b) \cup (-a, 0) \\ \pi\sigma & \xi \in (-b, -a) \end{cases} \quad \text{and} \quad q_{\text{s}} = \left(\frac{\xi + b}{\xi + a}\right)^{\sigma} = \left(\frac{\mathrm{e}^{-\phi} + b}{\mathrm{e}^{-\phi} + a}\right)^{\sigma}, \tag{4.6}$$

where the speed, $q_{\text{s}}$, follows from (A 3) and is then used in the boundary-integral equation (A 2$b$). This geometry corresponds to a step-up of angle $\pi\sigma > 0$ to the horizontal, and reversing the flow or allowing a step-down is straightforward. Such step-geometries have been considered by, e.g. [9,26] and they provide a canonical mathematical model for free surface channel flow. Examples of works studying other similar flows include [19,27–29].

In what follows, we must take care to transform the integration variables from $w$ to $\zeta$. We will abuse notation, and instead of writing $\chi(w) = \chi(-\log\zeta) \equiv X(\zeta)$, we write $\chi(\zeta)$ for $X(\zeta)$. Using (4.5) and (4.6) with $q_0 = q_{\text{s}}$, the analogous integrals to (3.1) and (3.2) are given by

$$I(\xi) = \int_{\text{A}}^{\xi} \tilde{f}(t)\mathrm{e}^{\chi(t)/\epsilon}\,\mathrm{d}t \quad \text{with } \chi(\zeta) = -\mathrm{i}\int_{-a}^{\zeta} \left(\frac{t+a}{t+b}\right)^{3\sigma} \left(-\frac{1}{t}\right)\mathrm{d}t, \tag{4.7}$$

written now for the $\zeta$-plane, and where we have defined $\tilde{f}(t) \equiv -f(\varphi)/\zeta$. The dummy variable is now $t$ corresponding to integration in the $\zeta$-plane. We have also defined $\chi$, so that $\chi(-a) = 0$, and this changes only the numerical pre-factors embedded in $\tilde{f}$. Like the example of the ship, it is convenient to consider the initial point of integration, $t = \text{A}$, at a finite non-degenerate point along the free-surface, $t \geq 0$. We will eventually let $\text{A} \to \infty$ so as to impose the natural boundary condition that requires uniform flow upstream, or $\bar{q} \to 0$ as $\zeta = \xi \to \infty$.

Consider now the rectangular step and set $\sigma = 1/2$ in (4.7). Within the integral for the $\chi$, we choose both branch cuts from $\zeta = -b$ and $\zeta = -a$ to lie in the direction of the positive real axis; owing to the combination of powers, this is equivalent to a single branch cut between the two points. There is a further logarithmic branch cut that arises from the pole at $\zeta = 0$.

Using the procedure described in §3, we generate the Riemann surface for $\chi$, and plot its projection into $(\mathrm{Re}\,\zeta, \mathrm{Im}\,\zeta, \mathrm{Re}\,\chi)$-space in figure 5. Recall the index notation of (3.6). In this case, the Riemann sheets are denoted by $\chi_{(k_1,k_2,k_3)}$ for the winding numbers associated with $\zeta = Z_i = \{-b, -a, 0\}$. The main sheet, $\chi_{(0,0,0)}$, is shown at the very top of the surface in figure 5. Also shown are two adjacent sheets, $\chi_{(0,0,1)}$ and $\chi_{(0,0,2)}$, achieved by passing through the logarithmic branch cut once or twice, respectively.

Examine now the lowest plane of figure 5, where several representative steepest ascent/descent (or constant-phase) curves have been projected down from the surface. Dashed constant phase lines emerge from $\zeta = -a$ and form two homoclinic orbits, separating the plane into three regions. The local angle of emergence of these contours can be determined by setting $\zeta + a \sim r\mathrm{e}^{\mathrm{i}\vartheta}$ and $\mathrm{Im}\,\chi = 0$ in (4.7). Within the interior of the right-most homoclinic (formed by angles $\vartheta = \pm\pi/5$), the constant phase paths form closed orbits that become increasingly circular

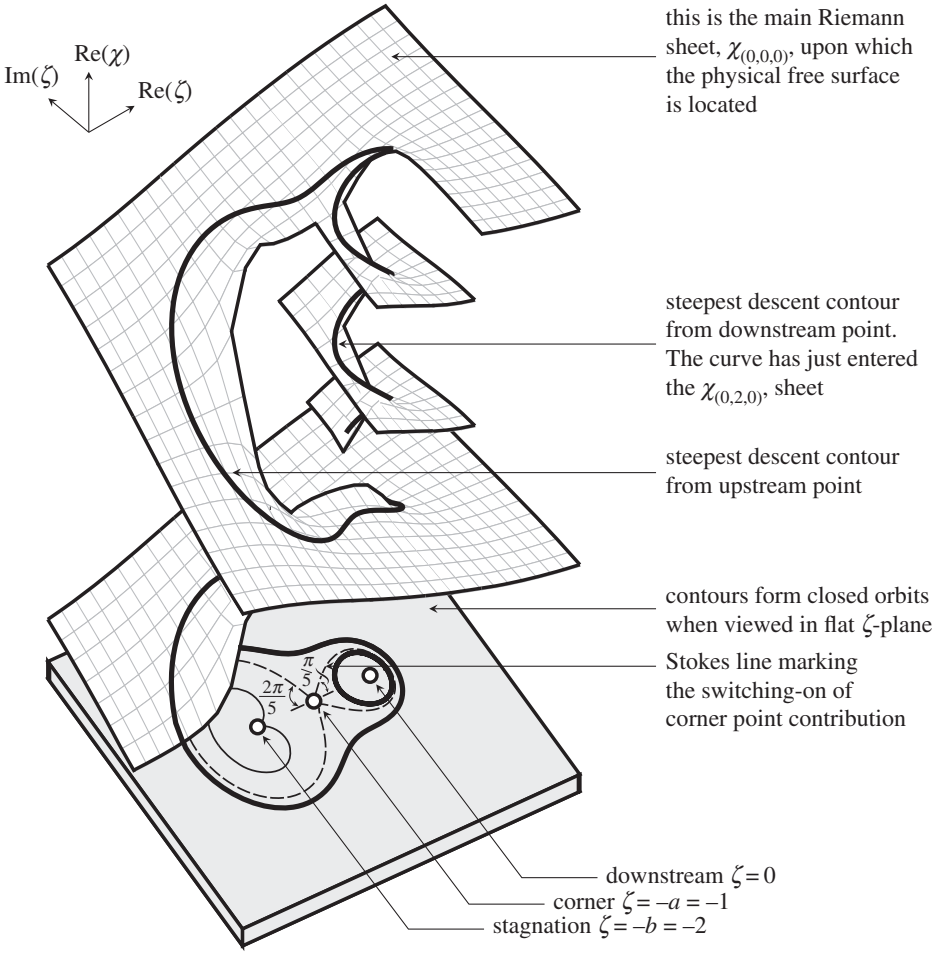


**Figure 5.** Riemann surface of $\chi$ for the rectangular step geometry with $\sigma = 1/2$, as shown in the (Re $\zeta$, Im $\zeta$, Re $\chi$)-plane. The three critical points are $\zeta = Z_i = \{-b, -a, 0\}$, where $b = 2$ and $a = 1$. The Riemann sheets are labelled $\chi_{(k_1,k_2,k_3)}$ for the respective winding numbers, $k_i$. The two thick contours correspond to steepest descent trajectories for an upstream and downstream point on the free surface. The lower plane shows the projection of curves onto the (Re $\zeta$, Im $\zeta$)-plane, with dashed lines indicating the contour Im $\chi = 0$ from $\zeta = -a$. The surface is generated from numerical integration of (4.7). Data and further visualizations of the surface are found in the electronic supplementary material.

near $\zeta = 0$. The left-most homoclinic is formed by angles $\vartheta = \pm 3\pi/5$. Outside both homoclinic orbits, the constant phase paths also form close contours, approximately in the shape of a figure eight. The other critical point at $\zeta = -b$, which corresponds to the stagnation point, is not a saddle–point of the integrand.

### (i) Only endpoint contributions

We now seek to deform the initial contour of integration of (4.7) in the case where the endpoints, $t = \mathrm{A}$ and $t = \xi = \mathrm{B}$, are both chosen sufficiently far upstream so as to lie outside the right homoclinic. The process of approximating the integral using the method of steepest descents is sketched in figure 6*a*. In the figure, we use $\zeta$ and $t$ interchangeably (the latter is a dummy variable).

Although the steepest descent paths from each individual point, A and B, form a closed orbits in the plane, each full anticlockwise rotation about the figure eight trajectory is accompanied by a smaller value of Re $\chi$. This is seen in the three-dimensional plot of figure 5. Thus, the final

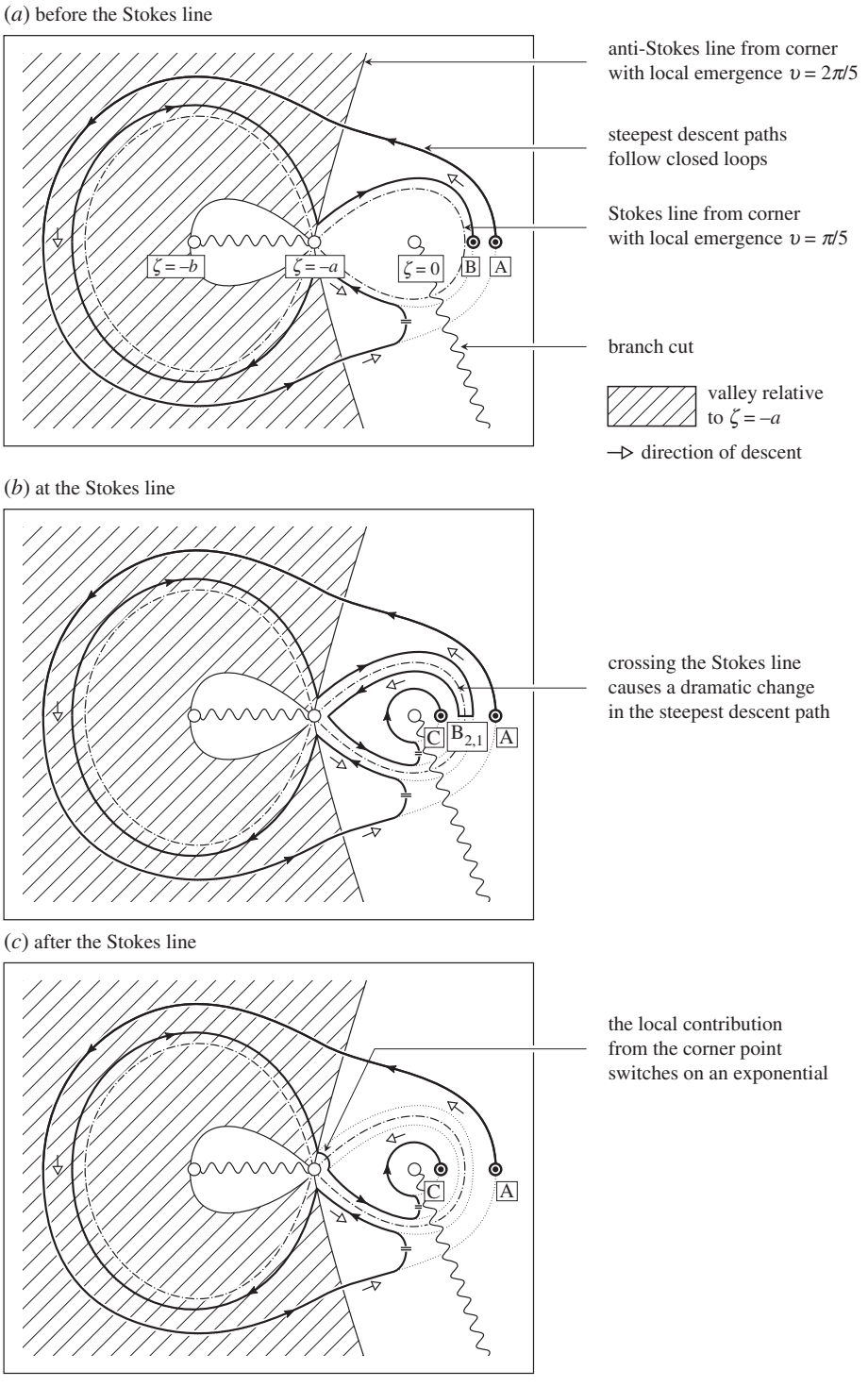


**Figure 6.** Illustration of steepest descent deformations for the rectangular step integral (4.7), as viewed in the (Re $\zeta$, Im $\zeta$)-plane (for dummy integration variable $t$). The endpoints of the contour are marked as a dark circle, and run from A to B in (*a*), or A to C in (*b*, *c*). Branch cuts are shown as a wavy line. The open circles indicate the three critical points $\zeta = Z_i = \{-b, -a, 0\}$. Black arrows along the thick lines indicate the integration direction, whereas white arrows indicate the local direction of descent. Note that the steepest descent process will continue to deform the curves marked by a double bar past the branch cuts, so that they eventually form closed orbits along the dotted curves.

deformed contour begins from A, and follows the trajectory anticlockwise, achieving smaller and smaller values of $\mathrm{Re}\,\chi$. In order to connect to the figure-eight contour joined to B, the connection is made within the valley where $\mathrm{Re}\,\chi \to -\infty$. Once done, the contour unwinds in a clockwise direction, and finally joins with B. Predictably, the result of this process is (4.2), and thus $I$ is approximated by the two endpoint contributions. This yields the regular asymptotic expansion of the solution.

Once we have understood this deformation process, it is simple to take the initial point $\mathrm{A} \to \infty$, that is, to be upstream infinity. We require the physical wave problem to impose a radiation condition such that the flow is uniform upstream and consequently, the only contribution to the integral at leading order is from an expansion about the point B.

*For points sufficiently far upstream of the step, we conclude that there are no free-surface waves in the* $\epsilon \to 0$ *limit.*

### (ii) Crossing the Stokes line

Now consider the deformation process when the initial contour of integration of (4.7) between $t = \mathrm{A}$ and $\xi = t = \mathrm{C}$ is chosen, so that C lies sufficiently far downstream and hence within the right-most homoclinic orbit. This is shown in figure 6*b*. We split the integration range in an analogous manner to (4.3), with points $t = \mathrm{B}_1$ and $\mathrm{B}_2$, chosen to lie just on the exterior and interior, respectively, of the homoclinic orbit. The critical dividing curve (the Stokes line), shown dash-dotted in the figure 6 is the constant phase line from the step corner, $t = -a$.

The steepest descent process then proceeds similarly as for the case of the rectangular ship: endpoint contributions are obtained from A and C, and a saddle–point contribution is obtained from the corner of the step. Unlike the steepest descent paths for the ship, which tend towards either $t = 0$ or $t = \infty$, the steepest descent paths for the rectangular step form closed orbits, with each rotation diminishing the value of the integrand. This is shown most clearly in the three-dimensional surface of figure 5.

*For points sufficiently far downstream from the rectangular step, we conclude that the free-surface waves arise from switching-on the saddle–point contribution owing to the corner of the step* (*the Stokes phenomenon*).

## (c) The angled step in a channel

In both the rectangular ship and rectangular step, we have shown how the intersection of a single Stokes line with the free-surface may account for the production of water waves. In more exotic geometries, multiple points in the body may produce multiple relevant Stokes lines.

Let us take, for instance, a step inclined at a shallow angle of $\pi\sigma = \pi/10$ to the horizontal. For this example, both $\zeta = -a$ and $\zeta = -b$ in (4.7) produce relevant Stokes lines that intersect the free surface. The Riemann surface for $\chi$ is shown in figure 7, and the picture reveals remarkable complexity, even for this moderately simple geometry. In contrast to the simpler rectangular step, steepest descent contours now travel past the branch cut associated with $\zeta = -b$, and move onto the sheet $\chi_{(-1,0,0)}$.

The steepest descent process will go through three possible configurations, depending on the extent in which $\xi$ in (4.7) lies downstream of the obstruction. If $\xi$ has not yet passed the first Stokes line from the corner, $\zeta = -a$, then only endpoint contributions are derived, and there are no waves in the limit $\epsilon \to 0$. Once $\xi$ passes the first Stokes line intersection from the corner, a single free-surface wave is switched on. Then, once $\xi$ passes the second Stokes line, a second wave is switched on. Thus, for this, $\xi$ chosen sufficiently far downstream, (4.4) is approximated as

$$I(\xi) \sim I_{\mathrm{endpt}} + I_{\mathrm{exp,stag}} + I_{\mathrm{exp,corner}} = I_{\mathrm{endpt}} + \left( \oint_{t=-b} + \oint_{t=-a} \right) \tilde{f}(t) \mathrm{e}^{\chi(t)/\epsilon} \mathrm{d}t, \tag{4.8}$$

where $I_{\mathrm{endpt}}$, $I_{\mathrm{exp,stag}}$ and $I_{\mathrm{exp,corner}}$ denote local contributions near the endpoints, stagnation point and corner point, respectively. The analytical forms of these terms follow from [8]. Note from (2.7)

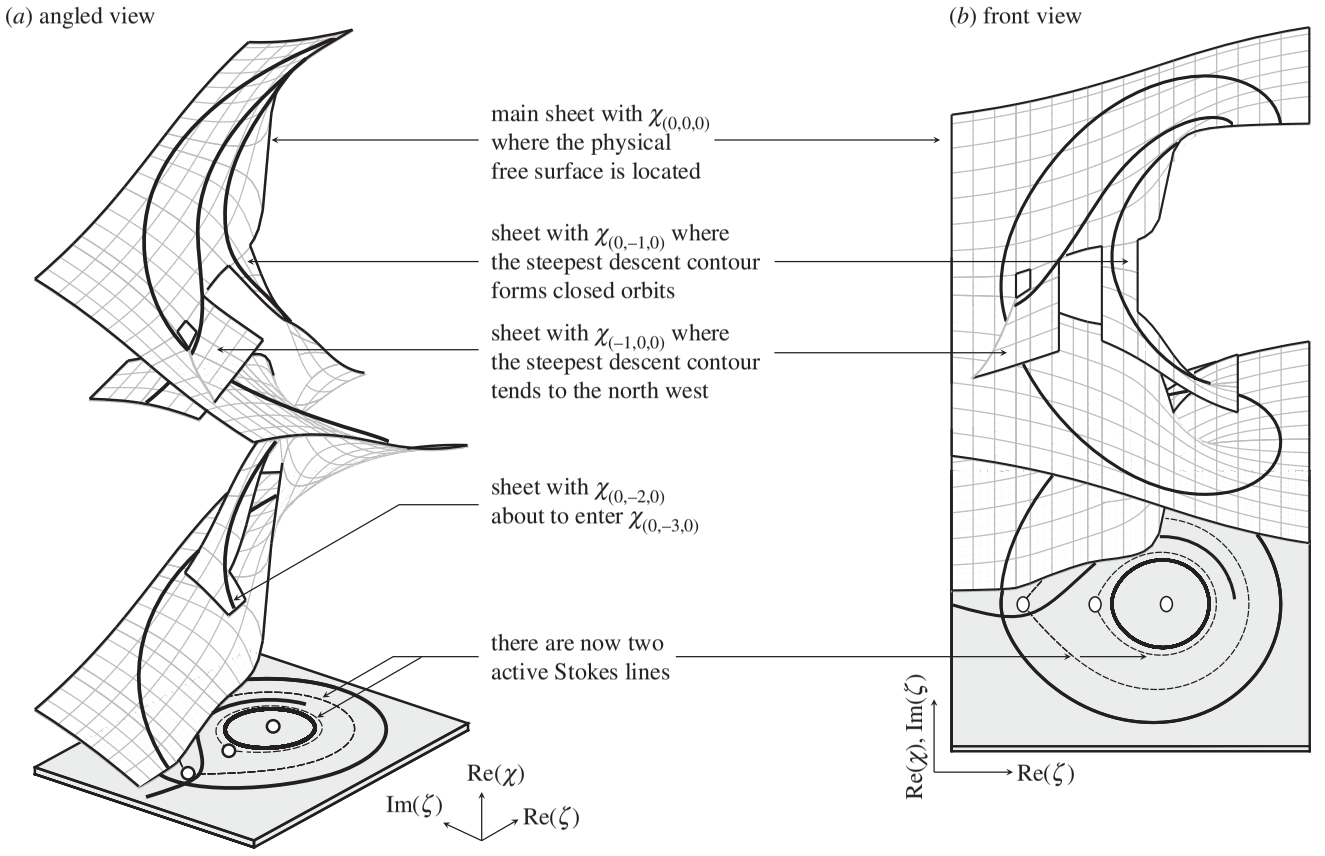


**Figure 7.** Riemann surface of $\chi$ for the angled step with $\sigma = 1/10$, as shown in the (Re $\zeta$, Im $\zeta$, Re $\chi$)-plane. The individual sheets are denoted by $\chi_{(k_1,k_2,k_3)}$ associated with the indices, $k_i$, for $\zeta = Z_i = \{-2, -1, 0\}$, for the step stagnation point, corner point and downstream infinity, respectively. Three thick contours correspond to steepest descent trajectories for three selected points on the free surface. The lower plane shows the projection of curves onto the (Re $\zeta$, Im $\zeta$)-plane, with dashed lines indicating the constant Im $\chi$ contours from $\zeta = -2$ and $-1$. The surface is generated from numerical integration of (4.7). Data and further visualizations of the surface are found in the electronic supplementary material.

that the wave amplitudes are proportional to $e^{-\mathrm{Re}\,\chi/\epsilon}$. Examination of the relative heights of Re $\chi$ in figure 7 then confirms that the free-surface waves generated by $t = -a$ (the stagnation point) are exponentially subdominant to those generated by $t = -b$ (the corner).

## 5. Discussion

The work in this paper was driven by two principal motivations.

The first motivation was to return to the work of Tulin [12] and Tuck [13,30], both of whom had proposed the reduced models for the study of free-surface flows with moving bodies. Their models shared common elements: for example, both authors had proposed a simplification of the Hilbert transform, and both emphasized the importance of analytic continuation of the real flow variables into the complex plane. However, the models were also incomplete, and thus the search for a complete model led to the companion work [8]. In this latter work, a systematic reduction of the water-wave equations demonstrates why certain simplifications can be applied in the low-Froude limit. There, the analysis depends on a general steepest descent argument, attributing surface waves to saddle–point contributions. Despite the relative simplicity of such arguments, the actual deformation process can be quite non-trivial. In this paper, our objective was to demonstrate how this steepest descent analysis is performed on concrete flow problems.

Our second motivation was to provide a powerful and visual methodology for the study of wave–structure interactions. This method establishes a correspondence between flow in the physical plane, with the topology of certain Riemann surfaces containing the paths of steepest descent. The theory is geometrically nonlinear and makes no assumption on the dimensions of the perturbing body; as explained in Introduction, such theories provide powerful tools for studying bluff-bodied interactions.

*Is it possible to consider other problems where a similar visual methodology is developed?* We are equally driven by the need to better understand free-surface waves produced by flow over nonlinear geometries under the effects of both gravity and surface tension. It is well known that in the case of gravity–capillary flows, the equivalent exponential asymptotics is a great deal more complicated [31,32]. More generally, the study of time-dependent or multi-dimensional problems using exponential asymptotics continues to pose significant challenges [33–36], particularly for the case of nonlinear phenomena.

*What other geometries can be studied using this approach?* The reader may remark that, in reality, ships or channel topographies may not be piecewise-linear in shape as they are considered here. In our work, the generation of waves is attributed to critical points in the geometry (corners or stagnation points), but surely a smooth object will still create a wave pattern! In fact, our analysis does not stipulate that the body must contain singularities *par se*, but rather that the analytic continuation of $q$ and $\theta$ must do so.

Consider, for example, the replacement of the bottom topography in figure 4 by any streamline of the flow above the step. The free-surface waves must necessarily remain the same and the analysis by the method of steepest descents must still apply as the (now-hidden) complex singularities of the step remain in place. Hence, there is no contradiction. Recent developments of powerful conformal mapping techniques for potential flow problems with multiply-connected regions also suggest the intriguing possibility of studying free-surface flows of a much wider class of problems (see e.g. work by Crowdy [37]). Finally, we note that our work here also suggests the possibility of studying flows past bodies with singularities weaker than the branch points found in the ship and step flows. In a forthcoming paper, a theory will be presented for flows past bodies with singularities in the curvature, rather than the angle.

Ethics. This work did not involve research on humans.

Data accessibility. Videos and data for the Riemann surfaces and surface plots are available within the electronic supplementary material. All remaining data accompanying this publication are directly available within the publication and are generated using standard routines in MATLAB.

Authors' contributions. I did all the work.

Competing interests. I have no competing interests.

Funding. I am grateful for financial support from Lincoln College, Oxford.
Acknowledgements. Drafts of this manuscript were completed during the author's visit to the Department of Mathematics at Duke University. I am most grateful for the exceedingly generous hospitality and encouragement of Prof. Thomas Witelski during this time.

## Appendix A. Governing equations

The general framework for the study of steady irrotational two-dimensional free-surface waves past a moving body is presented in the companion paper [8], and we also refer readers to the textbook by Vanden-Broeck [19] for a more extensive review. Here, we summarize the basic equations.

We begin with a set-up of the three relevant coordinate systems. First, the physical plane with $z = x + \mathrm{i}y$ is chosen, so that the body, which is moving at dimensional speed $U$, is fixed in a travelling frame of reference. Second, in the complex potential plane with $w = \phi + \mathrm{i}\psi$, the free surface is assumed to lie at $\psi = 0$ and the fluid region in $\psi < 0$. In the case of the semi-infinite surface-piercing flow, the body lies on $\phi < 0$ and the free-surface on $\phi > 0$, and a stagnation point attachment is assumed at $\phi = 0$. For channel flow, the fluid is confined within a finite strip, say $-\pi \leq \psi \leq 0$, with $-\infty < \phi < \infty$. The non-dimensional depth of the strip is chosen to be $\pi$ for convenience.

The third coordinate system is required only for the case of channel flow. Here, an additional mapping,

$$\zeta = \xi + \mathrm{i}\eta = \mathrm{e}^{-w}, \tag{A 1}$$

brings the fluid region to the upper half-$\zeta$-plane. The channel bottom now lies on $\xi < 0$, and the free surface on $\xi > 0$. For consistency of notation for the case of surface-piercing flows, we also consider the lower half-$\zeta$-plane, using the identity map $\zeta = w$. The relevant coordinate systems are shown in figures 1 (for the ship) and 4 (for the step).

A boundary-integral formulation of the potential flow equations yields the following system of equations for $q$ and $\theta$ along the free surface:

$$\epsilon q^2 \frac{\mathrm{d}q}{\mathrm{d}\phi} + \sin\theta = 0 \tag{A 2a}$$

and

$$\log q = \frac{\mathrm{j}}{\pi} \int_0^\infty \frac{\theta(\xi')}{\xi' - \xi} \mathrm{d}\xi' = \log q_\mathrm{s} + \mathrm{j}\mathscr{H}[\theta](\xi). \tag{A 2b}$$

The first, (A 2*a*), corresponds to Bernoulli's equation, and imposes a constant pressure condition on the surface. The second, (A 2*b*), involves a Cauchy principal value integral, and is equivalent to the imposition of Laplace's equation in the fluid region; it thus provides a second relationship between $q$ and $\theta$ that closes the system. In equation (A 2*b*), we have split the integral between the negative real axis (the body) and the positive real axis (the free surface), and defined the *body function* $q_\mathrm{s}$ and the Hilbert transform operator $\mathscr{H}$ according to

$$\log q_\mathrm{s} = \frac{\mathrm{j}}{\pi} \int_{-\infty}^0 \frac{\theta(\xi')}{\xi' - \xi} \mathrm{d}\xi' \quad \text{and} \quad \mathscr{H}[\theta](\xi) = \frac{1}{\pi} \int_0^\infty \frac{\theta(\xi')}{\xi' - \xi} \mathrm{d}\xi'. \tag{A 3a,b}$$

Above, we furthermore introduce the sign function

$$\mathrm{j} = \begin{cases} 1 & \text{for surface-piercing flow,} \\ -1 & \text{for channel flow,} \end{cases} \tag{A 4}$$

which accounts for the fact that, in the surface-piercing geometry, the in-fluid-region lies to the right of the free-surface for increasing $\xi$, but to the left for channel flows.

A given body geometry can be specified by providing the values of $\theta$ over $\xi < 0$. Then, by evaluating the integral (A 3*a*), a body function $q_\mathrm{s}$ is obtained that encodes the appropriate geometry. Note that when $\epsilon = 0$, $\theta = 0$ from (A 2*a*), and thus $q = q_\mathrm{s}$. This is the leading-order solution of a perturbative expansion $q = q_0 + \epsilon q_1 + \cdots$ and thus, $q_0 = q_\mathrm{s}$.

## (a) Reduction of water wave equations to integral form

We also summarize the main reduction of the water wave equations (A 2) to the integral form. The full details of this reduction can be found in [8].

The first step is to analytically continue the free surface quantities $q(\phi, \psi = 0)$ and $\theta(\phi, \psi = 0)$ into the complex $\phi$ (or $\xi$ plane). We thus set $\phi \mapsto \phi_r + \mathrm{i}\phi_c$ and $\xi \mapsto \xi_r + \mathrm{i}\xi_c$. Owing to the correspondence between the (physical) complex velocity $w = \phi + \mathrm{i}\psi$ (with $\phi, \psi \in \mathbb{R}$) and the new complexified $\phi$, we can relabel the analytic continuations to use $w$, with a similar relabelling for $\zeta$. Thus, we write $q(\phi, \psi = 0) \mapsto q(w)$ and $\theta(\phi, \psi = 0) \mapsto \theta(w)$. This step of analytic continuation is explained in more detail in [21,38], and the reader is also encouraged to see the visualization in fig. 2 of Trinh & Chapman [32]. Under this analytic continuation, the boundary-integral equation (A 2*b*) becomes

$$\log q + \mathrm{ij}\theta = \log q_\mathrm{s} + \mathrm{j}\hat{\mathscr{H}}[\theta], \quad \text{where } \hat{\mathscr{H}}[\theta](\zeta) = \frac{1}{\pi}\int_0^\infty \frac{\theta(\xi')}{\xi' - \zeta}\mathrm{d}\xi', \tag{A 5}$$

for analytic continuation into the upper half-$w$ or $\zeta$-plane.

The solutions, $q$ and $\theta$, are then expressed in terms of a regular series expansion with an error term, i.e. $q = q_r + \bar{q}$, $\theta = \theta_r + \bar{\theta}$ as in (2.4). Note that the leading-order $q_0$ is given by $q_\mathrm{s}$ in (A 3*a*) and $\theta_0 = 0$, known as the rigid-body flow. The combination of Bernoulli's equation (A 2*a*) and the boundary-integral equation (A 5) gives the result of reference [8]

**Result A.1 (reduced integrodifferential model).** Linearizing the water wave equations about a regular series expansion truncated at $N$ terms gives the following integrodifferential equation for the perturbation,

$$\epsilon\bar{q}' + [\chi'(w) + \epsilon P_1'(w) + \mathcal{O}(\epsilon^2)]\bar{q} = R(w; \hat{\mathscr{H}}[\bar{\theta}]) + \mathcal{O}(\bar{\theta}^2, \bar{q}^2), \tag{A 6a}$$

where

$$\chi(w) = \int_{w_0}^{w} \frac{\mathrm{ij}}{q_0^3(\varphi)}\mathrm{d}\varphi, \tag{A 6b}$$

$$\mathrm{e}^{-P_1(w)} = q_0^2(w^*)Q(w) = \left[\Lambda\frac{q_0^2(w^*)}{q_0^2(w)}\right]\exp\left(3\mathrm{ij}\int_{w^*}^{w}\frac{q_1(\varphi)}{q_0^4(\varphi)}\mathrm{d}\varphi\right) \tag{A 6c}$$

and

$$R(w; \hat{\mathscr{H}}[\bar{\theta}]) = -\mathcal{E}_\mathrm{bern} - \mathrm{ij}\mathcal{E}_\mathrm{int}\frac{\cos\theta_r}{q_r^2} + \mathrm{i}\hat{\mathscr{H}}[\bar{\theta}]\frac{\cos\theta_r}{q_r^2}, \tag{A 6d}$$

and the error term, $\mathcal{E}_\mathrm{bern}$, represents the error in Bernoulli's equation, and is given by

$$\mathcal{E}_\mathrm{bern} = \epsilon q_r' + \frac{\sin\theta_r}{q_r^2}. \tag{A 6e}$$

and the error term, $\mathcal{E}_\mathrm{int}$, in the integral equation is given by

$$\mathcal{E}_\mathrm{int} = \log q_r + \mathrm{ij}\theta_r - (\log q_0 - \mathrm{j}\hat{\mathscr{H}}[\theta_r]). \tag{A 6f}$$

The initial point of integration, $w_0$, in (A 6*b*) is typically chosen at an (integrable) singularity of $q_0$, given by (A 3*a*). The point of integration, $w^*$, can be chosen anywhere the integral in (A 6*c*) is defined, and only changes the constant of integration, $\Lambda$.

The solution of the first-order differential equation (A 6*a*) can then be written as the integral in (2.7). The initial point of integration is taken so as to satisfy the boundary or radiation conditions. For the case of the ship (2.5), we set $\phi_\mathrm{start} = 0$ (for the stagnation point), whereas for the case of the step, we set $\phi_\mathrm{start} = -\infty$ (for a wave-free upstream flow).

As discussed in reference [8], different choices for $R$ can be used in order to obtain different approximations to the waves. A particularly convenient and often very accurate choice is the

two-term approximation,

$$R(w;\hat{\mathscr{H}}[\bar{\theta}]) \sim -\epsilon^2\left(-\frac{5\mathrm{i}\mathrm{j}q_1^2}{2q_0^4}+q_1'+2\mathrm{i}\frac{\hat{\mathscr{H}}[\theta_1]q_1}{q_0^3}\right), \tag{A 7}$$

which was used to illustrate the numerical example of figure 1. A comparison of different choices for $R$ is presented in table 2 of Trinh [8].

## References


1. Tuck EO. 1964 A systematic asymptotic expansion procedure for slender ships. *J. Ship Res.* **8**, 639–668.
2. Wexler JS, Trinh PH, Berthet H, Quennouz N, du Roure O, Huppert HE, Linder A, Stone HA. 2013 Bending of elastic fibres in viscous flows: the influence of confinement. *J. Fluid Mech.* **720**, 517–544. (doi:10.1017/jfm.2013.49)
3. Darmon A, Benzaquen M, Raphaël E. 2014 Kelvin wake pattern at large Froude numbers. *J. Fluid Mech.* **738**, R3. (doi:10.1017/jfm.2013.607)
4. Pethiyagoda R, McCue SW, Moroney TJ. 2014 What is the apparent angle of a Kelvin ship wave pattern? *J. Fluid Mech.* **758**, 468–485. (doi:10.1017/jfm.2014.530)
5. Vanden-Broeck J-M. 1980 Nonlinear stern waves. *J. Fluid Mech.* **96**, 603–611. (doi:10.1017/S0022112080002273)
6. Ogilvie TF. 1968 Wave resistance: the low speed limit. Technical report 002, Michigan University, Ann Arbor, MI.
7. Tulin MP. 2005 Reminiscences and reflections: ship waves, 1950–2000. *J. Ship Res.* **49**, 238–246.
8. Trinh PH. 2016 On reduced models for gravity waves generated by moving bodies. *J. Fluid Mech.* (http://arxiv.org/abs/1510.06647)
9. Chapman SJ, Vanden-Broeck J-M. 2006 Exponential asymptotics and gravity waves. *J. Fluid Mech.* **567**, 299–326. (doi:10.1017/S0022112006002394)
10. Olde Daalhuis AB, Chapman SJ, King JR, Ockendon JR, Tew RH. 1995 Stokes phenomenon and matched asymptotic expansions. *SIAM J. Appl. Math.* **55**, 1469–1483. (doi:10.1137/S0036139994261769)
11. Chapman SJ, King JR, Adams KL. 1998 Exponential asymptotics and Stokes lines in nonlinear ordinary differential equations. *Proc. R. Soc. Lond. A* **454**, 2733–2755. (doi:10.1098/rspa.1998.0278)
12. Tulin MP. 1983 An exact theory of gravity wave generation by moving bodies, its approximation and its implications. In *Proc. 14th Symp. on Naval Hydrodynamics, Ann Arbor, Michigan, 23–27 August 1982*, pp. 19–51. National Academy Press.
13. Tuck EO. 1991 Waveless solutions of wave equations. In *Proc. 6th Int. Workshop on Water Waves and Floating Bodies*. Wood's Hole, MA: MIT Press.
14. Costin O. 2008 *Asymptotics and Borel summability*, vol. 141. Boca Raton, FL: Chapman & Hall/CRC.
15. Grimshaw R. 2010 Exponential asymptotics and generalized solitary waves. In *Asymptotic methods in fluid mechanics: survey and recent advances*, pp. 71–120. New York, NY: Springer.
16. Berry M. 1991 Asymptotics, superasymptotics, hyperasymptotics... In *Asymptotics beyond all orders* (ed. H Segur), pp. 1–14. Berlin, Germany: Springer.
17. Boyd JP. 1999 The devil's invention: asymptotic, superasymptotic and hyperasymptotic series. *Acta Appl. Math.* **56**, 1–98. (doi:10.1023/A:1006145903624)
18. Trinh PH, Chapman SJ, Vanden-Broeck J-M. 2011 Do waveless ships exist? Results for single-cornered hulls. *J. Fluid Mech.* **685**, 413–439. (doi:10.1017/jfm.2011.325)
19. Vanden-Broeck J-M. 2010 *Gravity-capillary free-surface flows*. Cambridge, UK: Cambridge University Press.
20. Vanden-Broeck J-M, Schwartz LW, Tuck EO. 1978 Divergent low-Froude-number series expansion of nonlinear free-surface flow problems. *Proc. R. Soc. Lond. A* **361**, 207–224. (doi:10.1098/rspa.1978.0099)
21. Trinh PH, Chapman SJ. 2014 The wake of a two-dimensional ship in the low-speed limit: results for multi-cornered hulls. *J. Fluid Mech.* **741**, 492–513. (doi:10.1017/jfm.2013.589)
22. Farrow DE, Tuck EO. 1995 Further studies of stern wavemaking. *J. Austral. Math. Soc. B* **36**, 424–437. (doi:10.1017/S0334270000007475)

23. Chapman SJ, Trinh PH, Witelski TP. 2013 Exponential asymptotics for thin film rupture. *SIAM J. Appl. Math.* **73**, 232–253. (doi:10.1137/120872012)
24. Crew SC, Trinh PH. 2016 New singularities for Stokes waves. *J. Fluid Mech.* **798**, 256–283. (doi:10.1017/jfm.2016.309)
25. Trinh PH. 2010 Exponential asymptotics and Stokes line smoothing for generalized solitary waves. In *Asymptotic methods in fluid mechanics: survey and recent advances* (ed. H. Steinrück), pp. 121–126. New York, NY: Springer.
26. King AC, Bloor MIG. 1987 Free-surface flow over a step. *J. Fluid Mech.* **182**, 193–208. (doi:10.1017/S0022112087002301)
27. Forbes LK, Schwartz LW. 1982 Free-surface flow over a semicircular obstruction. *J. Fluid Mech.* **114**, 299–314. (doi:10.1017/S0022112082000160)
28. Binder BJ, Blyth MG, McCue SW. 2013 Free-surface flow past arbitrary topography and an inverse approach for wave-free solutions. *IMA J. Appl. Math.* **78**, 685–696. (doi:10.1093/imamat/hxt015)
29. Lustri CJ, McCue SW, Binder BJ. 2012 Free surface flow past topography: a beyond-all-orders approach. *Eur. J. Appl. Math.* **1**, 1–27. (doi:10.5923/j.am.20110101.01)
30. Tuck EO. 1991 Ship-hydrodynamic free-surface problems without waves. *J. Ship Res.* **35**, 277–287.
31. Trinh PH, Chapman SJ. 2013 New gravity–capillary waves at low speeds. Part 1: linear theory. *J. Fluid Mech.* **724**, 367–391. (doi:10.1017/jfm.2013.110)
32. Trinh PH, Chapman SJ. 2013 New gravity–capillary waves at low speeds. Part 2: nonlinear theory. *J. Fluid Mech.* **724**, 392–424. (doi:10.1017/jfm.2013.129)
33. Lustri CJ, Chapman SJ. 2014 Unsteady flow over a submerged source with low Froude number. *Eur. J. Appl. Math.* **25**, 655–680. (doi:10.1017/S0956792514000217)
34. Howls CJ. 1997 Hyperasymptotics for multidimensional integrals, exact remainder terms and the global connection problem. *Proc. R. Soc. Lond. A* **453**, 2271–2294. (doi:10.1098/rspa.1997.0122)
35. Chapman SJ, Mortimer DB. 2005 Exponential asymptotics and Stokes lines in a partial differential equation. *Proc. R. Soc. A* **461**, 2385–2421. (doi:10.1098/rspa.2005.1475)
36. GL Body, JR King, RH Tew. 2005 Exponential asymptotics of a fifth-order partial differential equation. *Eur. J. Appl. Math.* **16**, 647–681. (doi:10.1017/S0956792505006224)
37. Crowdy D. 2012 Conformal slit maps in applied mathematics. *ANZIAM J.* **53**, 171–189. (doi:10.1017/S1446181112000119)
38. Trinh PH, Chapman SJ. 2015 Exponential asymptotics and problems with coalescing singularities. *Nonlinearity* **28**, 1229–1256. (doi:10.1088/0951-7715/28/5/1229)